ASCE

Influence of Process Variables on Shrinkage in Low-Calcium Fly-Ash Geopolymers

Mude Hanumananaik[1] and Kolluru V. L. Subramaniam[2]

Abstract: The influence of process variables such as curing temperature and relative humidity (RH) on the shrinkage of alkali-activated fly ash (AAF) is examined in this work. The ambient conditions are varied after an initial accelerated moist curing at high-temperature. An analysis interlinking the effects of curing on AAF strength, shrinkage, reaction product content, and porosity is performed. Strength achieved and the pore structure formed for the different curing conditions depend upon the sodium alumino-silicate (N-A-S-H) gel content formed in the AAF. While water is not directly combined in the formation of N-A-S-H gel, its content is sensitive to the availability of moisture. The moisture loss due to drying during the geopolymerization reduces the N-A-S-H content formed in the AAF. Compared to the continuous moist curing at elevated temperature, there is a decrease in the N-A-S-H content on lowering the temperature or drying produced by the decrease in RH. Reducing temperature and RH following initial accelerated curing has the beneficial effect of reducing the shrinkage compared to drying at a higher temperature. Reduction in the N-A-S-H content due to decrease in temperature after the accelerated curing is more significant than the drying on lowering the RH to 50%. The autogenous shrinkage measured under sealed conditions contributes significantly to the total shrinkage in AAF. The shrinkage in the AAF is significantly lower than a comparable cement paste. While shrinkage is produced by drying, the moisture loss and shrinkage relationship is not unique. The shrinkage produced by moisture loss due to drying is primarily influenced by the pore structure formed in the AAF, which also depends on the N-A-S-H content. The influences of temperature and humidity on the strength, pore structure and shrinkage are determined by the N-A-S-H formed in the AAF. **DOI: 10.1061/JMCEE7.MTENG-14761.**

Author keywords: Drying; Geopolymers; N-A-S-H; Porosity; Shrinkage.

Introduction

Fly-ash activated geopolymer binder is a viable alternative to the Portland cement for making concrete. Using fly ash to make geopolymer binders has environmental benefits besides allowing the efficient utilization of larger amounts than is achievable in traditional concrete mixes. In countries that have an increasing future demand for cement and concurrently a large projected volume of fly-ash production, these binders offer a sustainable solution to producing concrete. The microstructure and the final properties of the geopolymer depend on the source material and the activators used (Songpiriyakij et al. 2010; Chindaprasirt et al. 2012; Ryu et al. 2013; Aughenbaugh et al. 2014; Assi et al. 2016; Hajimohammadi and Deventer 2016; Leong et al. 2016; Bhagath Singh and Subramaniam 2018). Because low calcium fly ash is inexpensive and readily available, it is frequently chosen as the primary source material. Geopolymer made with low calcium fly ash has a lower energy cost associated with the production energy than Portland cement (Komljenović 2015). Additionally, it has comparable or higher compressive strength, better tolerance to sulfate attack, low creep, excellent acid resistance, and minimum shrinkage (Duxson et al. 2007; Habert et al. 2011; Mclellan et al. 2011; Pacheco-Torgal et al. 2012; Davidovits 2020).

Numerous studies have been conducted on the synthesis and chemistry of geopolymers formed using low calcium fly ash (Duxson et al. 2007; Bhagath Singh and Subramaniam 2017a, b, c). There is a relationship between the mechanical characteristics of geopolymers, such as their compressive strength, and the phase composition of the reaction product (Bhagath Singh and Subramaniam 2019a). Additionally, the composition of the activating solution necessary for reliably producing high strength geopolymers using fly ash of a given composition has been investigated (Bhagath Singh and Subramaniam 2020). It has been established that the reactive content in fly ash should determine the activating solution composition to produce the aluminosilicates of the composition, which can produce high strength. Typically, the reactive component of low calcium fly ash is a smaller fraction of total oxides in the fly ash (Bhagath Singh and Subramaniam 2018). Because of the low reactivity of low-calcium fly ash employed as source material, a high temperature is required for curing, making it appropriate for precast concrete applications. In precast applications, short-term curing at elevated temperatures is maintained. Quantifying the volumetric changes in the material are essential for producing crack-free precast element.

Volumetric changes in geopolymers are often associated with shrinkage during the formation of the reaction products or due to moisture and temperature changes following the curing. Volumetric changes have been identified with the formation of aluminosilicate gel during the geopolymerization (Wallah and Rangan 2006; Wongpa et al. 2010; Šmilauer et al. 2011). Previous studies have reported that the autogenous shrinkage of alkali activated fly ash based geopolymers predominantly occurred within the first few

[1]Research Scholar, Dept. of Civil Engineering, Indian Institute of Technology Hyderabad, Hyderabad, Telangana 502285, India. ORCID: https://orcid.org/0000-0002-0970-371X. Email: ce15m17p000001@iith.ac.in

[2]Professor, Dept. of Civil Engineering, Indian Institute of Technology Hyderabad, Hyderabad, Telangana 502285, India (corresponding author). ORCID: https://orcid.org/0000-0002-5995-0911. Email: KVLS@ce.iith.ac.in

Note. This manuscript was submitted on April 21, 2022; approved on October 14, 2022; published online on March 31, 2023. Discussion period open until August 31, 2023; separate discussions must be submitted for individual papers. This paper is part of the ***Journal of Materials in Civil Engineering***, © ASCE, ISSN 0899-1561.

days after casting (Ma and Ye 2015). Most previous studies have evaluated changes produced by drying after the curing. The drying shrinkage of alkali activated fly ash based geopolymers produced by moisture loss was smaller than OPC in preliminary investigation (Sagoe-Crentsil et al. 2013; Ma and Ye 2015; Thomas et al. 2017; Hojati et al. 2019; Gunasekera et al. 2019). After the initiation of drying, the rate of shrinkage in low calcium fly-ash geopolymer decreases rapidly, reaching equilibrium within seven days. The drying shrinkage of the alkali activated fly ash based geopolymers increases with a decrease in relative humidity (RH) (Hojati et al. 2019). Heat curing increases the rate of drying shrinkage, whereas the ultimate shrinkage strain is lower than that of room cured geopolymer paste (Thomas et al. 2017; Hojati et al. 2019). While the moisture loss from the alkali activated fly ash based geopolymer due to drying is linked to the shrinkage, the relationship between mass loss and shrinkage strain is complex as it is influenced by porosity and pore structure (Ma and Ye 2015; Ling et al. 2019; Hojati et al. 2019). The alkali-activated fly ash-based geopolymer's drying shrinkage behavior is affected by activator composition, such as the concentration of the NaOH and Na_2SiO_3/NaOH ratio and the activating solution/ binder ratio. It was found that an increase in the sodium and silica concentrations of the activating solution resulted in higher drying shrinkage of the alkali activated fly ash based geopolymer paste (Ma and Ye 2015). Mixtures with higher activator concentration and low modulus (SiO_2/Na_2O) exhibited higher drying shrinkage (Ling et al. 2019).

In previous studies, the curing conditions have varied in terms of the duration of high-temperature curing, between 1 day and 7 days (Hojati et al. 2019). Typically, accelerated curing involves short-term heat curing at high humidity. The temperature and humidity determine the moisture loss from the geopolymers, which influences the volumetric contraction. Drying also potentially influences the reaction product content and the microstructure formed in the hardened matrix. These factors are implicitly connected to the final strength attained by the geopolymer made from alkali-activated fly ash. The measured shrinkage should be correlated to the reaction product content in the activated mixtures to provide a consistent basis for evaluation. Understanding the interrelations between the temperature and humidity on gel formation, shrinkage, and porosity in an AAF paste is required. Delineating the influences of temperature and RH on the temporal evolution of shrinkage and strength are required for developing proper curing protocols. The is particularly critical for precast application, where elevated temperature curing is used.

This work investigates the shrinkage of geopolymers formed by alkali activation of low calcium fly ash for specialized short-term heat curing, such as that required for precast concrete applications. The activating solutions are proportioned for strength based on the amount of reactive content in fly ash for achieving aluminosilicates of consistent composition. The procedure developed previously for determining the activating solution composition for a given reactive oxide composition of fly ash was followed in determining the mixture compositions (Bhagath Singh and Subramaniam 2020). The measured volumetric change in the mixture produced by moisture loss and its impact on the reaction product content in the activated mixture are correlated.

Materials and Methods

Fly ash was activated with an alkaline solution, which was prepared by combining sodium hydroxide (NaOH) and sodium silicate ($Na_2O.xSiO_2$) solutions. The fly ash was collected from a 2,600 MW thermal power plant in Ramagundam, Telangana State, India. The oxide content of the fly ash and the particle size distribution of the fly ash were similar to the results reported previously (Reddy and Subramaniam 2021; Hanumananaik et al. 2022). The specific gravity and the LOI of the fly ash are 2.85 g/cm^3 and 1.05%, respectively. According to IS 3812 (BIS 2013) and ASTM C 618-19 (ASTM 2010), the fly ash meets siliceous and class F fly ash standards, respectively. Due to the low calcium content in the fly ash, siliceous fly ash is further subclassified as low-calcium fly ash.

The maximum strength achieved in the alkali-activated fly ash is determined by its reactive Al_2O_3 content (Bhagath Singh and Subramaniam 2020). The reactive silica content in the fly ash determines the extra silica required in the activating solution. An X-ray diffraction (XRD) analysis was used to identify the fly ash's reactive components. The typical XRD signature of fly ash is shown in Fig. 1. The Rietveld refinement process was used to identify the crystalline phases in the fly ash (Rietveld 1969; Hill and Howard 1987), as shown in Fig. 1. Quartz and Mullite are the primary crystalline components in fly ash. Smaller amounts of rutile, hematite, and magnetite are also found. The intensity signature of the glassy phase present in the fly ash is identified with a broad hump centered on $22.6 \pm 0.2\ 2\theta$. The reactive content of fly ash is present within its amorphous glassy phase (Bhagath Singh and Subramaniam 2016c).

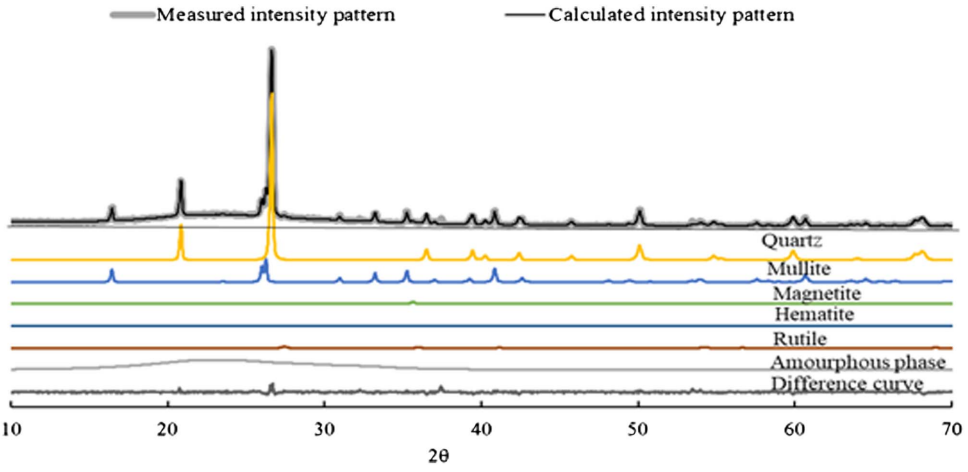

Fig. 1. Typical XRD spectrum of the low-calcium fly ash.

J. Mater. Civ. Eng., 2023, 35(6): 04023143

To quantify the reactive silica (SiO_2) and alumina (Al_2O_3) contents in the amorphous glassy phase, the quantities of these oxides in the known crystalline forms were subtracted from the total amounts of SiO_2 and Al_2O_3 in the fly ash. SiO_2 accounts for the entire mass of quartz and two-fifths of the mass fraction of mullite, according to stoichiometry. Mullite contains Al_2O_3, accounting for three-fifths of its mass fraction (Bhagath Singh and Subramaniam 2018). The total amorphous content and the individual reactive oxides of the fly ash are similar to those reported previously (Hanumananaik et al. 2022). Because of the low lime content and moderate to medium glassy content, the fly ash used in this study is typical of the fly ash produced in the Asian subcontinent (Bhagath Singh and Subramaniam 2018).

Commercially sourced sodium silicate and sodium hydroxide were used for preparing the alkali-silicate activating solution. The sodium silicate was supplied by Kiran Global Chemicals limited in a solution form and consisted of 14.70% sodium oxide (Na_2O), 34.17% silicon dioxide (SiO_2), and 51.13% water by mass. The specific gravity of the sodium silicate solution given by the supplier was 1.56 g/cm^3. The pH at 24°C and the silica modulus (modular ratio of SiO_2/Na_2O, M_S) of the sodium silicate solution were 12.98 and 2.32, respectively. The sodium hydroxide used was supplied by Thermo Fischer scientific as pellets of 99% purity. The activating solution was prepared using deionized water with a pH range of 7 to 7.1.

The alkali-activated fly ash (AAF) paste was prepared with a mass proportion of fly ash to activating solution (sol/b ratio) equal to 0.41 for workability. The activating solution used to prepare the AAF paste mixture was proportioned to achieve the highest strength with the lowest use of sodium hydroxide. The mass proportions of the AAF paste are listed in Table 1. In the AAF mixture, the reactive oxide ratios of SiO_2/Na_2O and SiO_2/Al_2O_3 were kept equal to 5.0 and 2.0, respectively. The reactive oxide ratios given in the table produce a sodium aluminosilicate (N-A-S-H) gel with a Si/Al ratio = 2.0 (Bhagath Singh and Subramaniam 2020). The reactive oxide ratios were determined considering the reactive SiO_2 and reactive Al_2O_3 available in the fly ash, and the external silica contributed by the activating solution. The minimum molarity of NaOH in the AAF paste was maintained at 3M, which was found to be adequate for the complete dissolution of the reactive content from the fly ash (Bhagath Singh and Subramaniam 2019a, 2020).

The influences of temperature and humidity in the curing period after subjecting the specimens to elevated temperature curing in the first 24 h were evaluated. Three different curing regimes were considered after 24 h and are listed in Table 2. The curing regimes were chosen depending on the precast use, where long-term heat curing in a moist environment is not feasible. In the 60C curing condition, the samples were continuously cured at 60°C and 95% relative humidity (RH). The curing regime was changed to 50% RH while maintaining the temperature at 60°C in the 60–60 curing condition. In the 60–30 curing condition, the AAF samples were subjected to 50% RH and 30°C after one day.

Table 1. Alkali-activated fly ash mixture composition

Component	Mass/quantity
$Na_2O.xSiO_2$ solution	179 g
NaOH	50 g
Added H_2O	179 g
NaOH molarity	4.22 M
Fly ash	1,000 g

Table 2. Different curing regimes

Curing condition	Curing regime	
	Up to 24 h	After 24 h
60C	95% RH and 60°C	60°C and 95%RH
60–60	95% RH and 60°C	50% RH and 60°C temperature
60–30	95% RH and 60°C	50% RH and 30°C temperature

Sample Preparation and Testing Methods

The sodium silicate and sodium hydroxide solutions were combined to make the alkali silicate activating solution. An 8M NaOH solution was made 24 h before mixing it with the sodium silicate solution. Additional water was added to the mix. A pan mixer was used to make the paste. Compressive strength was determined from standard 70 mm cube specimens. After casting, the cube molds were placed in an environmental testing chamber, maintained at 60°C and 95% RH for one day. The cubes were then exposed to different curing conditions, with the compressive strength measurements taken at 1, 3, 7, and 28 days following the standard test protocol given in IS 4031-part 6 (BIS 2005). Six cubes were tested at each age.

Prisms with 25 mm cross section and 285 mm length were used for drying shrinkage measurements following ASTM C596-18 (ASTM 2007). After demolding, initial measurements were taken using a 0.0025 mm accurate length comparator. After the initial reading, for the first 24 h, the length change was recorded every 2 h, and then one reading was recorded for one day. After measuring the length, mass loss was determined using a balance with 0.01 g accuracy. Measurements were performed on three companion specimens for each curing condition.

The autogenous shrinkage was measured using the corrugated pipe method prescribed in ASTM C 1698. A flexible corrugated pipe of a length of 420 ± 5 mm and a diameter of 29 ± 0.5 mm was used. After casting, both the ends of the corrugated pipes were sealed tightly with rubber corks, and the initial reading was recorded after the final setting time. Linear variable differential transformers (LVDT) with an accuracy of 0.001 mm were used to record the data at 50 s for the initial three days. The LVDTs were removed after three days, and the measurements were performed with a length comparator of 0.0025 mm accuracy for the remaining curing age.

A sample was collected from the core of the broken cube from compression testing for characterization studies. The sample was powdered, and the material passing through a 60-micron sieve was solvent exchanged in isopropanol. The sample was vacuum dried at 40°C to a constant weight and stored in air-tight vials.

XRD Measurements and Analysis

The Brucker D2 PhaserTM X-ray diffractometer equipped with an LYNXEYE compound silicon strip detector and Cu-Kα radiation source was used. A Soller 4° and an antiscatter slit of 8 mm were used for the diffracted beam. An air scatter screen was utilized to minimize the background noise. Measurements were obtained with a step size of 0.02° in a vertical Bragg-Brentano θ-θ goniometer over a range of 2θ angles between 10° and 70°. The samples were rotated at a rate of 15 rpm during the measurement to improve the accuracy and precision.

The background intensity was fitted using a Chebyshev polynomial with a $1/(2\theta)$ term (Snellings et al. 2014; Bhagath Singh and Subramaniam 2016a, b, c; Stetsko et al. 2017). The Rietveld refinement procedure was used for refining the intensity signature of each

crystalline phase with the crystalline structures provided by the International Center for Diffraction Data (ICDD). A NIST SRM 676a α-Al_2O_3 was used as an external standard for quantifying the crystalline phases using the external standard method. The mass percentage of each crystalline phase (w_{cp}) was determined as follows:

$$w_{cp} = \frac{(ZMV)_{cp} S_{cp} \mu_{sample}}{(ZMV)_s S_s \mu_s} w_s \times 100 \quad (1)$$

where Z = number of formula units in the unit cell, M = mass of the unit cell; S = scale factor; and V = volume of the unit cell. The subscript cp = crystalline phase, and s = the standard. μ_{sample} = the MAC of the sample, and μ_s = the MAC of the standard.

The glassy phase and N-A-S-H contents in the AAF samples with age were quantified. The direct decomposition method is an intensity-based procedure developed to quantify amorphous phases in AAF (Bhagath Singh and Subramaniam 2016c) and has recently been applied to alkali-activated slag (Reddy and Subramaniam 2020).

Mercury Intrusion Porosimetry (MIP)

The hardened AAF paste samples' porosity and pore size distribution were assessed using mercury intrusion porosimetry (MIP). MIP is commonly used in cementitious materials, and its use is extended to AAF. The Poremaster 60 porosimeter supplied by Quanta chrome was used for measurements. The measuring process was carried out in two steps. Initially, the sample cell was placed in a low-pressure port filled with mercury up to a pressure of 35 PSIA. In the next step, the sample was placed in the high-pressure port, and the pressure was applied over the range of 20 to 60,000 PSIA using hydraulic oil. At each pressure step, the pore size is determined using the Washburn equation, given as

$$D = \frac{-4\gamma \cos\theta}{P} \quad (2)$$

where D, γ, θ, and P = pore diameter (μm), the surface tension of the mercury (mN/m) (0.485 N/m), contact angle of mercury (140°), and applied pressure (MPa), respectively. The porosity from pores ranging in sizes from 1,100 μm to 3.6 nm was obtained from the intrusion measurement.

Results and Discussion

Fig. 2 shows the compressive strength of the AAF for the different curing conditions. There is a very rapid strength gain for all curing conditions up to 3 days, following which there is a steady, nearly linear increase up to 28 days. The rate of strength gain is influenced immediately after reducing the RH. Following a decrease in RH, there is a decrease in the strength gain. The differences between the curing at lower RH (60–60 and 60–30 curing regimes) and continuous moist curing (60C) develop up to 7 days. The rate of strength gain between 7 and 28 days is, however, comparable for all curing regimes. The 28-day strengths obtained from the two curing conditions at lower humidity, 60–60 and 60–30, are comparable. There is a 15%–20% decrease in the strength on lowering the RH when compared with continuous moist curing. As a reference, pastes made with cement and fly ash also exhibit similar dependence on RH (Warangkana et al. 2008). The decrease in strength in the hydraulic mixtures of cement and fly ash is also initiated immediately after commencement of drying. The decrease in the compressive strength is however significantly higher for cement paste subjected to lower RH (Warangkana et al. 2008). Typically, decreasing the RH to 50% produces a strength loss of 40% and higher in cement pastes.

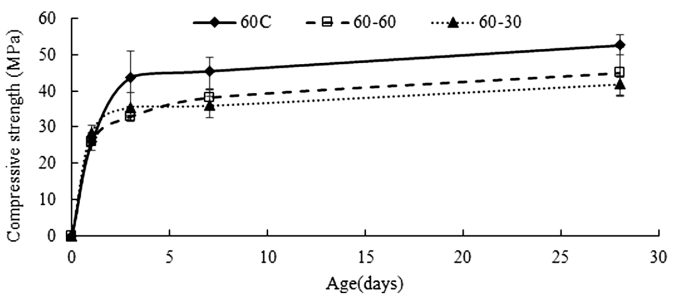

Fig. 2. Compressive strength of the AAF pastes for the different curing regimes.

Reaction Product Content

Fig. 3 shows a typical XRD intensity profile of the 28-day 60C AAF. The Rietveld refining process was used for the intensity signatures of the different crystal phases and is shown in Fig. 3. The crystalline phases seen in the AAF are essentially those present in the fly ash. New crystalline phases were identified in trace quantities. The Pawley refinement procedure was used to obtain the intensity signature of the total amorphous phase in the AAF (Pawley 1981) and is shown in Fig. 3. An hkl phase was defined for a cubic structure with $Fm\bar{3}m$ space group (space group No. 225) (Bhagath Singh and Subramaniam 2016c).

The intensity signature produced by the amorphous phase in AAF contains the contributions from the N-A-S-H formed in the AAF and from the unreacted fly-ash glassy phase. The amorphous phase is identified by a large hump with a substantial scattering in the 2θ range between 20° and 40°. The intensity signatures of the N-A-S-H and the unreacted fly ash were obtained using the direct decomposition method (Bhagath Singh and Subramaniam 2016c). The broad intensity signature of the total amorphous phase in the AAF was decomposed into underlying intensity signatures of the N-A-S-H and the unreacted glassy phase. Pseudo-Voigt (PV) peaks were fit to the total intensity signature following unconstrained non-linear optimization. Iterative least-squares fit for the intensity pattern was performed by varying the parameters of the PV functions. The intensity signatures of the glassy phase of fly ash and the N-A-S-H present in the AAF are shown in Fig. 3. The undissolved fly-ash glassy phase (labeled PV fit 1) creates a diffuse hump centered on 21.2 ± 0.2 2θ, while the diffuse scattering produced by N-A-S-H (labeled PV fit 2) results in a hump centered on 27.7 ± 0.2 2θ.

The N-A-S-H intensity signature obtained from the 28-day AAF paste subjected to continuous moist curing and the 60–60 and 60–30 curing conditions are shown in Fig. 4. The intensity signatures of N-A-S-H from all three curing conditions are nominally similar. While the individual amplitude of the intensity pattern produced by N-A-S-H changes with the curing conditions, the overall intensity pattern remains largely unaltered. This suggests that the drying and moisture loss do not alter the structure of the N-A-S-H formed in the AAF during the geopolymerization.

The intensity-based procedure was used to quantify the reaction product content within the AAF paste. The mass fraction of reaction product content is computed as the area contributed by the amorphous phase to the area of the total spectrum (Riello 2004). The amorphous phase as the percentage by mass is computed as (Madsen et al. 2011)

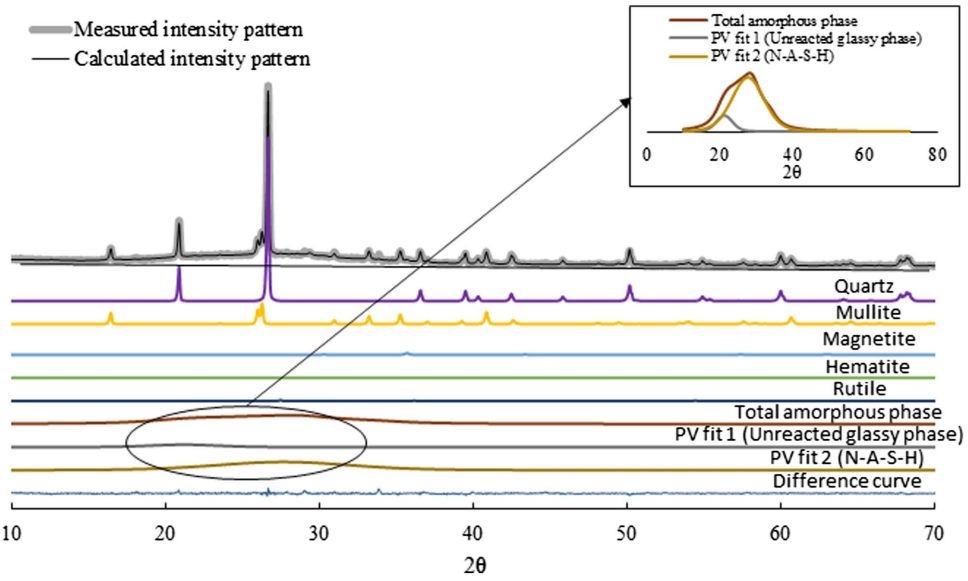

Fig. 3. Typical XRD intensity signature of the 60C AAF sample at 28 days.

$$\%\,amorphous = \left[\frac{Area\ under\ the\ intensity\ pattern\ of\ amorphous\ phase}{Total\ area\ under\ diffractogram}\right] \times 100 \quad (3)$$

Fig. 5 shows the N-A-S-H content in the AAF paste as a function of age. The N-A-S-H content as a function of age increases rapidly within the first 24 h. With time, there is a decrease in the N-A-S-H produced. In the continuously moist cured AAF, while the N-A-S-H content was 35% after 24 h, there was a further increase to 44% at 28 days. The N-A-S-H contents in the AAF for the 60–60 and 60–30 curing conditions decreased relative to the continuously moist cured samples. A comparable decrease in the N-A-S-H content is produced in samples cured at reduced humidity at 60°C and 30°C. Between 1 and 28 days, the N-A-S-H content increased from 35% to 38% for the 60–60 and 60–30 curing conditions. In an AAF paste, the N-A-S-H content depends on the temperature (Bhagath Singh and Subramaniam 2019b). Comparing 60–60 and 60–30, the degree of polymerization is expected to be lower at 30°C. The results, however, indicate that lowering the temperature is offset by another parameter, which appears to influence the N-A-S-H content in the AAF. As a reference, reducing the RH also produces a decrease in the degree of hydration reaction of cement with water. Decrease in RH resulted in reduced interlayer water content and reduced reaction product content (Cong and Kirkpatrick 1995; Warangkana et al. 2008). The degree of hydration in cement paste samples exhibits a higher sensitivity to the RH.

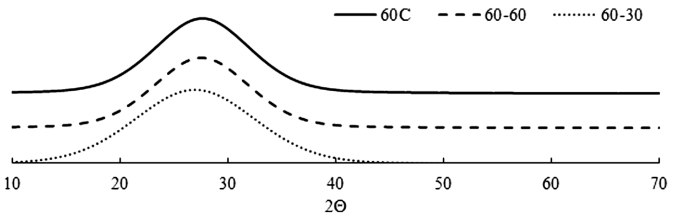

Fig. 4. Intensity of N-A-S-H in AAF cured at different curing regimes obtained using direct decomposition.

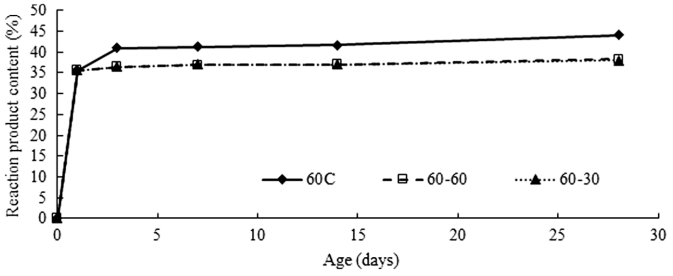

Fig. 5. Reaction product content in AAF for the different curing regimes.

Autogenous Shrinkage

Fig. 6 shows the autogenous shrinkage of AAF continuously cured at 60°C. Additionally, the autogenous shrinkage recorded from AAF cured at 30°C after curing at 60°C in the initial 24 h is also shown. Each data point represents the average of three replicates, and the range of results is shown using scatter bars. The autogenous shrinkage of ordinary Portland cement (OPC) paste with a water-to-cement ratio (w/c) of 0.41 cured at 30°C is also plotted in the figure for reference. The trends from the measurements indicate that the autogenous shrinkage in AAF was most prominent in the first 24 h, and it attained a constant value by 30 days. The incremental change after 24 h is, however, minimal. Similar results have also been reported previously, where the autogenous shrinkage in geopolymer pastes occurred within the first few days (Ma and Ye 2015). The volumetric contraction under the sealed conditions at 60°C is close to 550 $\mu\varepsilon$. In the sample cured at 30°C after 24 h, there is an abrupt increase in the measured autogenous shrinkage on lowering the temperature. This volumetric shrinkage recorded within a short time after lowering the temperature is associated with thermal contraction. The observed contraction contributes an additional 200 $\mu\varepsilon$ to the shrinkage under sealed conditions at 30°C. The incremental volumetric contraction after the specimens attains thermal equilibrium on reducing the temperature from 60°C to 30°C is essentially the same as that recorded from the specimens cured at

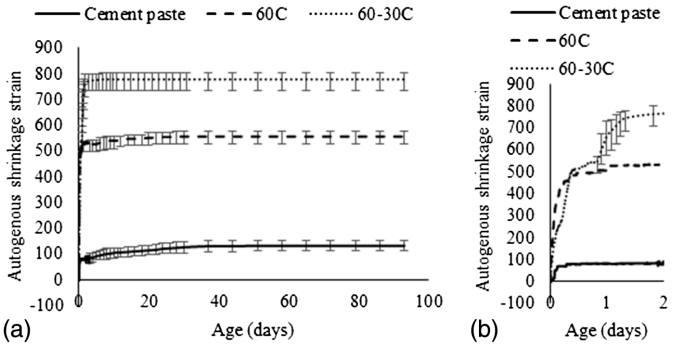

Fig. 6. Autogenous shrinkage of AAF at different curing temperatures: (a) up to 100 days; and (b) in the first 2 days.

60°C. The autogenous shrinkage recorded from the AAF paste is significantly higher than the autogenous shrinkage measured in cement paste. For cement paste with a w/c ratio of 0.41, the autogenous shrinkage is typically low, ranging between 100 and 130 $\mu\varepsilon$ (Baroghel-Bouny et al. 2006).

Drying Shrinkage and Mass Loss

Drying shrinkage and mass loss recorded from AAF subjected to the 60–60 and 60–30 curing conditions are shown in Fig. 7. Drying shrinkage measured from OPC pastes made with w/c = 0.41 and cured at 30°C is also shown for reference. The cement paste was demolded at 24 h and subjected to drying at 50% RH. The shrinkage recorded from the AAF and cement pastes up to 3 days were nominally identical. However, the continued shrinkage with time is significantly higher in cement paste when compared with AAF paste. While there is significant continued shrinkage in the cement paste up to 28 days, the additional shrinkage in AAF is lower. The drying shrinkage measured from the cement and AAF pastes at 28 days were 3,500 $\mu\varepsilon$, and 1,200 $\mu\varepsilon$, respectively. Most drying shrinkage in the AAF paste occurred within the first few days of starting the drying process. The shrinkage was essentially constant ten days after the initiation of drying. The drying shrinkage recorded from the 60–60 and the 60–30 curing conditions is similar. A constant difference of 200 $\mu\varepsilon$ between the drying shrinkage recorded from the two conditions occurs due to the additional thermal contraction in the 60–30 curing condition.

The mass loss recorded from the samples subjected to the different curing conditions is shown in Fig. 7(b). The mass loss was very rapid in the first few days after the initiation of drying following, which the value essentially becomes constant. In the case of AAF paste, the drying was very intense in the first seven days, which attained a constant value by 10 days. In the case of cement paste, intense drying indicated by mass loss occurred in the first four days after the initiation of drying. The drying rate slowed down and attained a constant value at 28 days. The total mass loss recorded from AAF paste was lower than the cement pastes, irrespective of the curing regime. Comparing the curing regimes, the mass loss from the AAF for the 60–60 curing condition was higher than the mass loss from the 60–30 curing. Mass loss of the OPC paste at 28 days was approximately 16%, and the mass losses of the AAF for the 60–60 and 60–30 curing were approximately 11.5% and 8%, respectively.

The mass loss recorded from the AAF paste indicates that the drying associated with moisture loss depends on both temperature and relative humidity. There was larger moisture loss on decreasing the RH to 50% at 60°C compared to 30°C. Due to the greater volatility of water at higher temperatures, the drying produced by the reduced relative humidity becomes more severe at a higher temperature. Water becomes more volatile, and the vapor pressure of liquid increases resulting in faster drying at a higher temperature (Zhang et al. 2021). The moisture loss and drying measured from the AAF pastes at two different temperature is consistent with the observations from cement paste. Data recorded from cement pastes have previously shown that the level of saturation achieved during the desorption depends on both temperature and humidity. With decreasing RH, a lower saturation level was produced at a higher temperature indicating a higher level of drying in the multiporous material such as cement paste (Zhang et al. 2021).

Porosity and Pore Structure

Fig. 8 depicts the porosity and pore structure in the 28-day AAF paste assessed using MIP according to Washburn's equation (Corp 2001). The total pore volumes accessed by the intrusion measurement in the AAF pastes cured at lower RH were significantly higher than the pore volume measured in the continuously moist cured AAF paste. The porosity of the AAF paste cured at 60–60 and 60–30 were similar over the range of pore sizes accessed by the intrusion measurement. Compared with the continuous moist curing, there was an increase in the pore volume over two size ranges in the AAF paste cured at lower humidity (60–60 and 60–30 curing regimes). There was a large difference in the volume of pores over the size ranges centered on 100–300 μm and 20–40 μm. Fig. 8(b) shows differential pore volume as a function of the pore diameter. The pore structure indicated by the differential volume indicates that the pores are present in two size ranges. The larger pores are present over the range of 100–300 μm. The critical pore diameters are identified over the size range 20–40 μm. Continuous moist

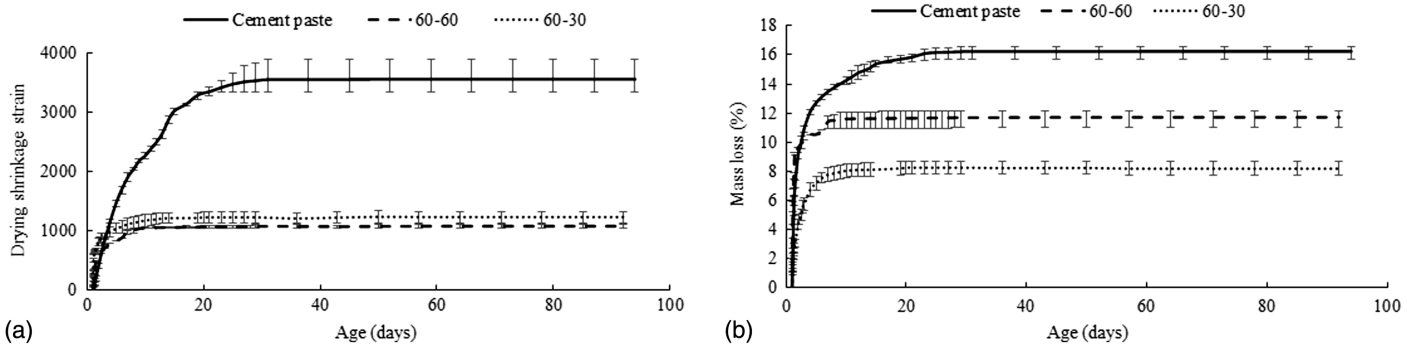

Fig. 7. (a) Drying shrinkage; and (b) mass loss measured from the AAF and OPC pastes.

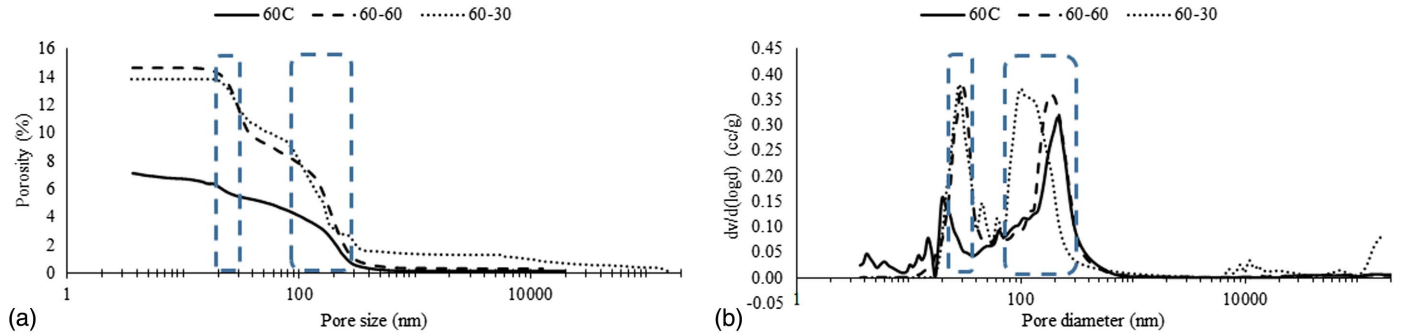

Fig. 8. (a) Porosity; and (b) pore size distribution in the 28-day AAF pates.

Table 3. Porosity and critical pore size of AAF cured at different curing regimes

Mix Id	Total porosity (%)	Critical pore size (nm)
60C	7.08	21.4
60–60	14.7	29.2
60–30	13.9	29.2

curing (60C) resulted in more N-A-S-H and denser pore structure than the other two curing regimes (60–60 and 60–30). The critical pore diameters for the 60–60 and 60–30 curing conditions are identical, and larger than the critical pore diameter in the continuously moist cured AAF. The total porosity and the critical pore size values are listed in Table 3.

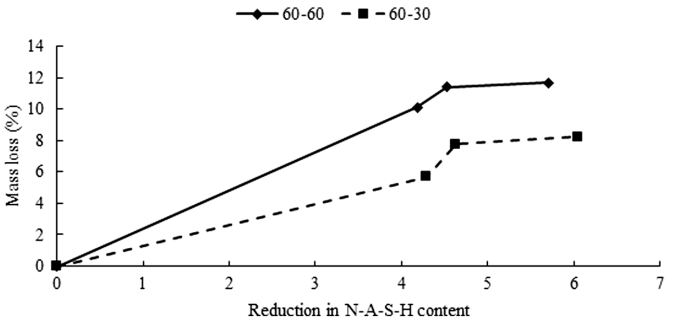

Fig. 9. Relationship between mass loss and reaction product content for the different curing conditions.

Discussion

Internal parameters such as activator composition and binder characteristics (Ma and Ye 2015; Hojati et al. 2019), and extrinsic ones like RH and curing temperature (Hojati et al. 2019) influence the shrinkage of AAF. The autogenous shrinkage recorded from the AAF paste under sealed conditions predominantly occurs within the first 24 h. As a result, no discernible variations were found in the shrinkage measured from the sealed specimens continuously cured at 60°C and from 60–30 curing (the sealed specimens were cured at 30°C after 24 h). Unlike cement paste, where the internal RH decreases due to internal desiccation produced by the binding of water in the CSH gel, the internal RH in AAF with progressing geopolymerization remains high (Ma and Ye 2015). In the case of the AAF paste, the continuous reorganization and polymerization of the aluminosilicate gel produce autogenous volume change (Wallah and Rangan 2006; Wongpa et al. 2010; Šmilauer et al. 2011; Ma and Ye 2015). Geopolymerization involves intermediate steps where the hydroxyl ions are bound with the precursors in the solution. The hydroxyl ion condensation, which occurs during the polymerization, releases water into the AAF. Water is not chemically bound within the geopolymer gel. The initial uptake of hydroxyl ions during geopolymerization produces the volumetric contraction. Additionally, the volumetric contraction under the sealed conditions may also be due to chemical shrinkage associated with the volume of reaction products compared to the initial volume of reactants.

The internal moisture content is important in the formation of AAF reaction products. When the ambient RH falls below 100%, the internal water starts evaporating, influencing the AAF reactions. While water is not directly involved in forming N-A-S-H, it is required as a medium for geopolymerization (Provis and Van Deventer 2009). The mass loss under the 60–60 curing condition is higher than the mass loss recorded in the 60–30 curing. However, the N-A-S-H contents in the AAF are identical for both 60–60 and 60–30 curing conditions. The larger mass loss from the samples subjected to 60–60 curing results in more internal drying. The reduction in water content impacts the formation of N-A-S-H when compared to the continuously moist cured samples.

The curing temperature influences N-A-S-H content in the AAF (Bhagath Singh and Subramaniam 2019b). Reducing the temperature decreases the N-A-S-H content in AAF. When the temperature is reduced from 60°C to 30°C in the 60–30 curing condition, the production of N-A-S-H is reduced. The correlation between the mass loss and the reduction in N-A-S-H content is shown in Fig. 9. The reduction in the N-A-S-H content was calculated relative to the continuously moist-cured AAF. Under the 60–60 curing, while an elevated temperature was maintained for continued geopolymerization, the severe drying reduces the amount of water present in the system for the reaction to progress. In 60–30 curing, even though the drying is less severe, the lower temperature slows the reaction. N-A-S-H content is limited by the insufficient water in the 60–60 curing and the lower temperature in the 60–30 curing. Comparing the 60–60 and the 60–30 curing conditions, reducing the temperature has a comparable influence on the N-A-S-H content as the loss of moisture produced by drying.

The free water evaporation from the hardened sample's pores produces drying shrinkage. The N-A-S-H content determines the total porosity in the AAF paste. Total porosity and N-A-S-H contents in the 28-day 60–60 and 60–30 cured AAF pastes are identical. The continually moist cured AAF paste has a greater N-A-S-H content, which results in a lower total porosity. The pore structure within the interconnected pores indicated by the MIP also

largely agrees with the N-A-S-H content. The critical pore size corresponding to 44% N-A-S-H content for the continuously moist cured paste was approximately 21 nm. For the 60–60 and the 60–30 samples, the critical pore diameter was 29 nm, while the N-A-S-H content was 38%.

The aluminosilicate gel pores have voids filled with free water (Lloyd et al. 2009). Evaporation of water from AAF paste results in the formation of a meniscus in partially saturated pores, which creates tensile strains. With a reduction in humidity, it is expected that the moisture loss in a porous system results in the formation of capillary tension, the migration of interlayer water, and the lowering of disjoining pressure (Beltzung and Wittmann 2005). Interestingly, while a higher moisture loss occurs when lowering the RH at a higher temperature (in the 60–60 curing condition), the drying shrinkage is identical to the value obtained at a lower temperature (60–30 curing condition). The porosity and pore structure for the 60–60 and 60–30 curing conditions are also nominally identical. Fig. 10 shows the relationship between reaction product content and total shrinkage strain of AAF for the different curing regimes. A nominally identical relationship between the N-A-S-H content in the AAF and the shrinkage is obtained from the different curing conditions. It is observed that there is a change in the relationship between the volumetric contraction and the N-A-S-H gel formed with increasing reaction product content. In the early stages, the autogenous shrinkage contributes significantly to the total shrinkage. Subsequently, with the onset of drying, the loss of moisture from the pore system produces shrinkage. However, the addition of gel after the start of drying is not significant. The relationship between the total shrinkage and the gel content in the AAF is identical for the 60–60 and the 60–30 curing conditions. While the gel contents are identical for the two curing conditions, the moisture loss is higher for the 60–60. The relationship between moisture loss and shrinkage is therefore not unique. Similar observations have been reported previously (Ma and Ye 2015; Hojati et al. 2019).

In a multiconnected porous material with a continuously varying pore network made of irregular pores, such as cement paste, the dominant pores are centered in two broad sizes ranging in μm and nm ranges (Cook and Hover 1999; Dong et al. 2017). Typically, a bimodal distribution of pores is assessed from most measurement techniques (Cook and Hover 1999; Bernardo et al. 2006). Desorption studies from cement pastes indicate the roles of temperature and humidity during the drying as a function of humidity and temperature. The desorption at lower RH from cement paste, associated with drying from pores of the smaller size range, is largely invariant with temperature (Zhang et al. 2021). The adsorption and desorption isotherms are similar at low RH values (below 50%). The desorption from the larger pores, which typically dry out over an RH range of 50%, exhibits a temperature dependence. Hysteresis between adsorption and desorption is created at moderate and high RH values and is largely associated with drying from pores in larger sizes. The adsorption and desorption at low RH are essentially associated with moisture movement in gel pores sizes 10 nm and smaller. The saturation levels during drying or capillary condensation in these gel pores exhibit a similar variation with RH, independent of temperature (Zhang et al. 2021). Typically, differences in the desorption curves up to 50% RH are seen. The values at and below 50% typically do not show variation with temperature.

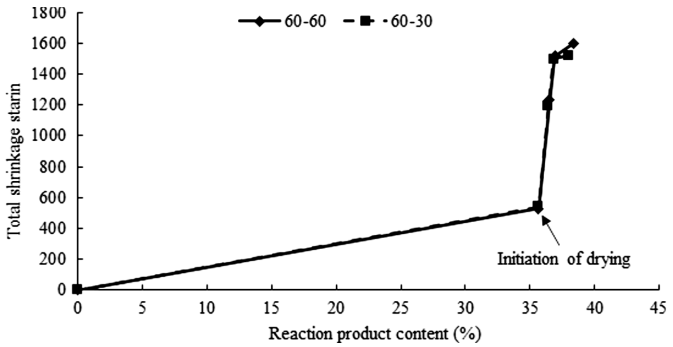

Fig. 10. Relationship between reaction product content and total shrinkage strain.

The drying from the porous network within the AAF produced by changes in humidity also exhibits a behavior similar to that observed in cement paste. The learnings from cement paste can be extended to explain the nonunique relationship between mass loss and shrinkage in AAF. The pore size ranges in AAF assessed using MIP are similar to those in hardened cement paste. The mass loss on lowering the RH is temperature-dependent, and it is associated with drying from the larger pores (μm-sized pores). The larger pores in the 100 μm range exhibit a temperature sensitivity to drying at 50% RH. On lowering the RH, a lower saturation of these pores is produced at a higher temperature. The desorption from the smaller pores (nm-sized pores) in the AAF does not exhibit temperature dependence on lowering the RH. The observed differences in the mass loss produced by drying are related to the larger pores' saturation levels. The drying of the smaller pores is largely unaffected by the temperature. The drying from the smaller pores controls the shrinkage. Therefore, while there is a difference in the mass loss from the 60–60 and the 60–30 curing conditions, the drying shrinkage is nearly identical. The volume change produced by drying is largely not influenced by the temperature used for accelerated curing of AAF.

For the accelerated curing at elevated temperature, significant AAF gel formation occurs within the first 24 h. This is suitable for use in precast operations. A significant shrinkage is produced from internal mechanisms associated with gel formation within the first 24 h. The magnitude of this autogenous shrinkage is comparable to the volumetric change produced by drying. In cement paste systems, the drying shrinkage contributes significantly to the total volumetric contraction. The autogenous shrinkage is significant only for highly reactive cementitious materials or low w/c ratios. Most of the considerations for shrinkage in design codes are calibrated for the expected volumetric change induced by the shrinkage. In AAF, shrinkage produced in the sealed conditions associated with gel formation is a significant proportion of the total shrinkage. However, the total shrinkage is smaller than the shrinkage from comparable cement paste.

The autogenous shrinkage is produced early, within the period of accelerated curing. The drying shrinkage is also very intense immediately following the initiation of drying. The direct application of available information on shrinkage from cement-based concrete would overpredict the magnitude and duration of drying shrinkage. The overall shrinkage produced by drying is lower in AAF, leading to fewer problems with restrained shrinkage cracking or prestress losses. However, the shrinkage under sealed conditions, which occurs with the formation of the N-A-S-H gel, needs to be quantified and accounted for since this cannot be mitigated by curing.

Conclusions

This study evaluated the influence of process variables on the shrinkage produced in AAF. Changes in the volume measured for the different RH and temperature conditions are related with the

changes in the reaction product content and microstructure in the hardened AAF. The following are the key findings of this study

- The process variables such as curing temperature and relative humidity (RH) play a crucial role in the mechanical and physical properties of AAF. Compared to the continuous moist curing at elevated temperature, the compressive strength decreased by 15% in the 60–60 and 60–30 curing regimes. The compressive strength of the different curing regimes depends on the N-A-S-H content and the pore structure created in the AAF. A decrease in the temperature leads to a reduction in the N-A-S-H content. The N-A-S-H content formed in the AAF also decreases if there is moisture loss due to drying.
- The moisture loss produced by drying depends on the RH and the curing temperature. A higher mass loss is produced on drying at 50% RH and 60°C when compared with drying at 50% RH and 30°C.
- The reduction in the N-A-S-H content produced by the additional drying in the 60–60 curing condition is comparable to the decrease in the N-A-S-H content produced by the decreased temperature in the 60–30 curing.
- The pore structure in the AAF depends only on the N-A-S-H content. The porosity and the critical pore diameters in the AAF are similar for the 60–60 and the 60–30 curing regimes.
- The shrinkage in the AAF paste subjected to initial accelerated moist curing at an elevated temperature is significantly lower than a comparable cement paste. Autogenous shrinkage produced under sealed conditions contributes significantly to the total shrinkage in the AAF. The drying shrinkage on reducing the RH and temperature after the initial moist curing at elevated temperature is influenced by both temperature and RH. Reduced temperature and RH contribute to a decrease in the N-A-S-H gel content in the AAF. Reducing the curing temperature is more significant for the N-A-S-H gel content than the drying on lowering RH when both temperature and RH are decreased. The 60–30 curing resulted in N-A-S-H gel content, comparable to the 60–60 curing regime. There is lesser moisture loss, and the resulting decrease in the N-A-S-H content is, therefore, the influence of reduced temperature.

Data Availability Statement

Some or all data, models, or codes that support the findings of this study are available from the corresponding author upon reasonable request.

Acknowledgments

The lead author would like to acknowledge support from the Ministry of tribal affairs, India, under the scheme "National Fellowship and Scholarship for Higher Education of ST students."

References

Assi, L., S. A. Ghahari, E. E. Deaver, D. Leaphart, and P. Ziehl. 2016. "Improvement of the early and final compressive strength of fly ash-based geopolymer concrete at ambient conditions." *Constr. Build. Mater.* 123 (Oct): 806–813. https://doi.org/10.1016/j.conbuildmat.2016.07.069.

ASTM. 2007. *Standard test method for drying shrinkage of mortar containing hydraulic cement*. ASTM C596-18. West Conshohocken, PA: ASTM.

ASTM. 2010. *Standard specification for coal fly ash and raw or calcined natural pozzolan for use*. ASTM C618-19. West Conshohocken, PA: ASTM.

Aughenbaugh, K. L., T. Williamson, and M. C. G. Juenger. 2014. "Critical evaluation of strength prediction methods for alkali-activated fly ash." *Mater. Struct./Materiaux et Constr.* 48 (3): 607–620.

Baroghel-Bouny, V., P. Mounanga, A. Khelidj, A. Loukili, and N. Rafaï. 2006. "Autogenous deformations of cement pastes: Part II. W/C effects, micro-macro correlations, and threshold values." *Cem. Concr. Res.* 36 (1): 123–136. https://doi.org/10.1016/j.cemconres.2004.10.020.

Beltzung, F., and F. H. Wittmann. 2005. "Role of disjoining pressure in cement-based materials." *Cem. Concr. Res.* 35 (12): 2364–2370. https://doi.org/10.1016/j.cemconres.2005.04.004.

Bernardo, G., A. Telesca, and G. L. Valenti. 2006. "A porosimetric study of calcium sulfoaluminate cement pastes cured at early ages." *Cem. Concr. Res.* 36 (6): 1042–1047. https://doi.org/10.1016/j.cemconres.2006.02.014.

Bhagath Singh, G. V. P., and K. V. L. Subramaniam. 2016a. "Direct decomposition X-ray diffraction method for amorphous phase quantification and glassy phase determination in binary blends of siliceous fly ash and hydrated cement." *J. Sustainable Cem.-Based Mater.* 6 (2): 111–125. https://doi.org/10.1080/21650373.2016.1177478.

Bhagath Singh, G. V. P., and K. V. L. Subramaniam. 2016b. "Method for direct determination of glassy phase dissolution in hydrating fly ash-cement system using x-ray diffraction." *J. Am. Ceram. Soc.* 100 (1): 403–412. https://doi.org/10.1111/jace.14486.

Bhagath Singh, G. V. P., and K. V. L. Subramaniam. 2016c. "Quantitative XRD study of amorphous phase in alkali activated low calcium siliceous fly ash." *Constr. Build. Mater.* 124 (Oct): 139–147. https://doi.org/10.1016/j.conbuildmat.2016.07.081.

Bhagath Singh, G. V. P., and K. V. L. Subramaniam. 2017a. "Evaluation of sodium content and sodium hydroxide molarity on compressive strength of alkali activated low-calcium fly ash." *Cem. Concr. Compos.* 81 (Aug): 122–132. https://doi.org/10.1016/j.cemconcomp.2017.05.001.

Bhagath Singh, G. V. P., and K. V. L. Subramaniam. 2017b. "Role of reactive alumina and reactive oxide ratios on strength development in alkaline activation of low-calcium fly ash." In Vol. 2 of *Proc., Int. Conf. on Advances in Construction Materials and Systems*, 243–250. Paris: RILEM Publications SARL.

Bhagath Singh, G. V. P., and K. V. L. Subramaniam. 2017c. "Role of total reactive oxide ratios on strength development in activated fly ash." In *Proc., Int. Conf. on Advances in Sustainable Construction Materials & Civil Engineering Systems (ASCMCES-17)*. Les Ulis, France: EDP Sciences. https://doi.org/10.1051/matecconf/201712002014.

Bhagath Singh, G. V. P., and K. V. L. Subramaniam. 2018. "Characterization of Indian fly ashes using different experimental techniques." *Indian Concr. J.* 92 (3): 10–23.

Bhagath Singh, G. V. P., and K. V. L. Subramaniam. 2019a. "Effect of active components on strength development in alkali-activated low calcium fly ash cements." *J. Sustainable Cem.-Based Mater.* 8 (1): 1–19. https://doi.org/10.1080/21650373.2018.1520657.

Bhagath Singh, G. V. P., and K. V. L. Subramaniam. 2019b. "Influence of processing temperature on the reaction product and strength gain in alkali-activated fly ash." *Cem. Concr. Compos.* 95 (Oct): 10–18. https://doi.org/10.1016/j.cemconcomp.2018.10.010.

Bhagath Singh, G. V. P., and K. V. L. Subramaniam. 2020. "Evaluation of total reactive oxide ratios and working solution ratios on strength development in fly ash–based geopolymers." *J. Mater. Civ. Eng.* 32 (4): 04020051. https://doi.org/10.1061/(ASCE)MT.1943-5533.0003109.

BIS (Bureau of Indian Standards). 2005. *Methods of physical tests for hydraulic cement Part 6: Determination of compressive strength of hydraulic cement other than masonry cement (first revision)*. IS: 4031. New Delhi, India: BIS.

BIS (Bureau of Indian Standards). 2013. *Specification for Pulverized fuel ash, Part-1: For use as Pozzolana in cement, cement mortar and concrete*. IS:3812. New Delhi, India: BIS.

Chindaprasirt, P., U. Rattanasak, P. Vongvoradit, and S. Jenjirapanya. 2012. "Thermal treatment and utilization of Al-rich waste in high calcium fly

ash geopolymeric materials." *Int. J. Miner. Metall. Mater.* 19 (9): 872–878. https://doi.org/10.1007/s12613-012-0641-z.

Cong, X., and R. J. Kirkpatrick. 1995. "Effects of the temperature and relative humidity on the structure of CSH gel." *Cem. Concr. Res.* 25 (6): 1237–1245. https://doi.org/10.1016/0008-8846(95)00116-T.

Cook, R. A., and K. C. Hover. 1999. "Mercury porosimetry of hardened cement pastes." *Cem. Concr. Res.* 29 (6): 933–943. https://doi.org/10.1016/S0008-8846(99)00083-6.

Corp, M. I. 2001. "An introduction to the physical characterization of materials by mercury intrusion porosimetry with emphasis on reduction and presentation of experimental data Paul A. Webb Norcross, Georgia." *Mercury* 22 (Jan): 1–23.

Davidovits, J. 2020. *Geopolymer chemistry and applications*. 5th ed. Saint-Quentin, France: Institut Géopolymère.

Dong, H., P. Gao, and G. Ye. 2017. "Characterization and comparison of capillary pore structures of digital cement pastes." *Mater. Struct./Mater. Constr.* 50 (2): 1–12. https://doi.org/10.1617/s11527-017-1023-9.

Duxson, P., A. Fernández-Jiménez, J. L. Provis, G. C. Lukey, A. Palomo, and J. S. J. Van Deventer. 2007. "Geopolymer technology: The current state of the art." *J. Mater. Sci.* 42 (9): 2917–2933. https://doi.org/10.1007/s10853-006-0637-z.

Gunasekera, C., S. Setunge, and D. W. Law. 2019. "Creep and drying shrinkage of different fly-ash-based geopolymers." *ACI Mater. J.* 116 (1): 39–49. https://doi.org/10.14359/51706941.

Habert, G., J. B. D'Espinose De Lacaillerie, and N. Roussel. 2011. "An environmental evaluation of geopolymer based concrete production: Reviewing current research trends." *J. Cleaner Prod.* 19 (11): 1229–1238. https://doi.org/10.1016/j.jclepro.2011.03.012.

Hajimohammadi, A., and J. S. J. van Deventer. 2017. "Characterisation of one-part geopolymer binders made from fly ash." *Waste Biomass Valorization* 8 (1): 225–233. https://doi.org/10.1007/s12649-016-9582-5.

Hanumananaik, M., M. S. K. Reddy, and K. V. L. Subramaniam. 2022. "High-temperature performance of low-calcium fly ash–based geopolymers." *J. Mater. Civ. Eng.* 34 (5): 04022040. https://doi.org/10.1061/(ASCE)MT.1943-5533.0004181.

Hill, R. J., and C. J. Howard. 1987. "Quantitative phase analysis from neutron powder diffraction data using the Rietveld method." *J. Appl. Crystallogr.* 20 (6): 467–474. https://doi.org/10.1107/S0021889887086199.

Hojati, M., F. Rajabipour, and A. Radlińska. 2019. "Effect of activator, curing and humidity on drying shrinkage of alkali-activated fly ash." *Green Mater.* 7 (2): 71–83. https://doi.org/10.1680/jgrma.18.00069.

Komljenović, M. 2015. "Mechanical strength and Young's modulus of alkali-activated cement-based binders." In *Handbook of alkali-activated cements, mortars and concretes*, 171–215. Cambridge, MA: Woodhead Publishing.

Leong, H. Y, D. E. L. Ong, J. G. Sanjayan, and A. Nazari. 2016. "The effect of different Na_2O and K_2O ratios of alkali activator on compressive strength of fly ash based-geopolymer." *Constr. Build. Mater.* 106 (Mar): 500–511. https://doi.org/10.1016/j.conbuildmat.2015.12.141.

Ling, Y., K. Wang, and C. Fu. 2019. "Shrinkage behavior of fly ash based geopolymer pastes with and without shrinkage reducing admixture." *Cem. Concr. Compos.* 98 (Feb): 74–82. https://doi.org/10.1016/j.cemconcomp.2019.02.007.

Lloyd, R. R., J. L. Provis, K. J. Smeaton, and J. S. J. van Deventer. 2009. "Spatial distribution of pores in fly ash-based inorganic polymer gels visualised by Wood's metal intrusion." *Microporous Mesoporous Mater.* 126 (1–2): 32–39. https://doi.org/10.1016/j.micromeso.2009.05.016.

Ma, Y., and G. Ye. 2015. "The shrinkage of alkali activated fly ash." *Cem. Concr. Res.* 68 (Feb): 75–82. https://doi.org/10.1016/j.cemconres.2014.10.024.

Madsen, I. C., N. V. Y. Scarlett, and A. Kern. 2011. "Description and survey of methodologies for the determination of amorphous content via X-ray powder diffraction." *Z. Kristallogr.* 226 (12): 944–955. https://doi.org/10.1524/zkri.2011.1437.

Mclellan, B. C., R. P. Williams, J. Lay, A. Van Riessen, and G. D. Corder. 2011. "Costs and carbon emissions for geopolymer pastes in comparison to ordinary portland cement." *J. Cleaner Prod.* 19 (9–10): 1080–1090. https://doi.org/10.1016/j.jclepro.2011.02.010.

Pacheco-Torgal, F., Z. Abdollahnejad, A. F. Camões, M. Jamshidi, and Y. Ding. 2012. "Durability of alkali-activated binders: A clear advantage over portland cement or an unproven issue?" *Constr. Build. Mater.* 30 (May): 400–405. https://doi.org/10.1016/j.conbuildmat.2011.12.017.

Pawley, G. S. 1981. "Unit-cell refinement from powder diffraction scans." *J. Appl. Crystallogr.* 14 (6): 357–361. https://doi.org/10.1107/S0021889881009618.

Provis, J. L., and J. S. J. Van Deventer. 2009. *Geopolymers Structure, processing, properties and industrial applications*. Oxford, UK: Woodhead Publishing Limited.

Reddy, K. C., and K. V. L. Subramaniam. 2020. "Quantitative phase analysis of slag hydrating in an alkaline environment." *J. Appl. Crystallogr.* 53 (2): 424–434. https://doi.org/10.1107/S1600576720001399.

Reddy, K. C., and K. V. L. Subramaniam. 2021. "Investigation on the roles of solution-based alkali and silica in activated low-calcium fly ash and slag blends." *Cem. Concr. Compos.* 123 (Jul): 104175. https://doi.org/10.1016/j.cemconcomp.2021.104175.

Riello, P. 2004. "Quantitative analysis of amorphous fraction in the study of the microstructure of semi-crystalline materials." In Vol. 68 of *Diffraction analysis of the microstructure of materials*, edited by E. J. Mittemeijer and P. Scardi. Berlin: Springer.

Rietveld, H. M. 1969. "A profile refinement method for nuclear and magnetic structures." *J. Appl. Crystallogr.* 2 (2): 65–71. https://doi.org/10.1107/S0021889869006558.

Ryu, G. S., Y. B. Lee, K. T. Koh, and Y. S. Chung. 2013. "The mechanical properties of fly ash-based geopolymer concrete with alkaline activators." *Constr. Build. Mater.* 47 (Oct): 409–418. https://doi.org/10.1016/j.conbuildmat.2013.05.069.

Sagoe-Crentsil, K., T. Brown, and A. Taylor. 2013. "Drying shrinkage and creep performance of geopolymer concrete." *J. Sustainable Cem.-Based Mater.* 2 (1): 35–42. https://doi.org/10.1080/21650373.2013.764963.

Šmilauer, V., P. Hlaváček, F. Škvára, R. Šulc, L. Kopecký, and J. Němeček. 2011. "Micromechanical multiscale model for alkali activation of fly ash and metakaolin." *J. Mater. Sci.* 46 (20): 6545–6555. https://doi.org/10.1007/s10853-011-5601-x.

Snellings, R., A. Salze, and K. L. Scrivener. 2014. "Use of X-ray diffraction to quantify amorphous supplementary cementitious materials in anhydrous and hydrated blended cements." *Cem. Concr. Res.* 64 (Oct): 89–98. https://doi.org/10.1016/j.cemconres.2014.06.011.

Songpiriyakij, S., T. Kubprasit, C. Jaturapitakkul, and P. Chindaprasirt. 2010. "Compressive strength and degree of reaction of biomass- and fly ash-based geopolymer." *Constr. Build. Mater.* 24 (3): 236–240. https://doi.org/10.1016/j.conbuildmat.2009.09.002.

Stetsko, Y. P., N. Shanahan, H. Deford, and A. Zayed. 2017. "Quantification of supplementary cementitious content in blended Portland cement using an iterative Rietveld-PONKCS technique." *J. Appl. Crystallogr.* 50 (2): 498–507. https://doi.org/10.1107/S1600576717002965.

Thomas, R. J., D. Lezama, and S. Peethamparan. 2017. "On drying shrinkage in alkali-activated concrete: Improving dimensional stability by aging or heat-curing." *Cem. Concr. Res.* 91 (Jan): 13–23. https://doi.org/10.1016/j.cemconres.2016.10.003.

Wallah, S. E., and B. V. Rangan. 2006. "Low calcium fly ash-based geopolymer concrete: Long-term properties." In *Research report GC 2 faculty of engineering*. Perth, WA, Australia: Curtin Univ. of Technology Perth.

Warangkana, S., T. Nawa, and P. Termkhajornkit. 2008. "Influence of relative humidity on compressive strength of fly ash cement paste." *J. Struct. Constr. Eng.* 73 (631): 1433–1441. https://doi.org/10.3130/aijs.73.1433.

Wongpa, J., K. Kiattikomol, C. Jaturapitakkul, and P. Chindaprasirt. 2010. "Compressive strength, modulus of elasticity, and water permeability of inorganic polymer concrete." *Mater. Des.* 31 (10): 4748–4754. https://doi.org/10.1016/j.matdes.2010.05.012.

Zhang, Q., Z. Kang, Y. Ling, H. Chen, and K. Li. 2021. "Influence of temperature on the moisture transport in concrete." *Crystals* 11 (1): 69. https://doi.org/10.3390/cryst11010069.